metals

MDPI

Article

Microstructural Evolution and Mechanical Properties of V-Containing Medium-Mn Steel Adopting Simple Intercritical Annealing

Cansheng Yu [1,2], Ning Zhao [3,4], Yu Mei [4], Weisen Zheng [4,*], Yanlin He [4], Lin Li [4] and Guo Yuan [1]

[1] State Key Laboratory of Rolling and Automation, Northeastern University, Shenyang 110819, China
[2] State Key Laboratory of Vanadium and Titanium Resources Comprehensive Utilization, Pangang Group Research Institute Co., Ltd., Panzhihua 617000, China
[3] School of Aeronautics and Mechanical Engineering, Changzhou Institute of Technology, Changzhou 213032, China
[4] State Key Laboratory of Advanced Special Steel, School of Materials Science and Engineering, Shanghai University, Shanghai 200444, China
* Correspondence: wszheng@shu.edu.cn; Tel.: +86-021-5633-1472

Abstract: The variations of the microstructure and mechanical properties of medium-Mn steel after vanadium (V) microalloying with different contents were investigated. After a one-step intercritical annealing (IA) at 730 °C, the steel containing 0.04 wt.% of V exhibited excellent comprehensive properties. The steel maintained an ultimate tensile strength (UTS) of 1000 MPa while also exhibiting a total elongation (TEL) of 37% and a product of strength and plasticity (PSE) of 37.7 GPa%. V-microalloying improved the yield strength (YS) and UTS of the experimental steel by refining ferrite grains and precipitation strengthening, however, it deteriorated its plasticity, which is difficult to compensate for through grain refinement and due to the TRIP effect of retained austenite (RA). The largest amount of RA and the appropriate stability also make a significant contribution to the outstanding UTS of the steel containing 0.04 wt.% of V through the TRIP effect. However, the further increase of V content led to decreased RA content and stability, weakening the TRIP effect and resulting in a weaker strength ductility balance.

Keywords: retained austenite; vanadium micro-alloying; medium-Mn steel; TRIP

Citation: Yu, C.; Zhao, N.; Mei, Y.; Zheng, W.; He, Y.; Li, L.; Yuan, G. Microstructural Evolution and Mechanical Properties of V-Containing Medium-Mn Steel Adopting Simple Intercritical Annealing. *Metals* **2024**, *14*, 144. https://doi.org/10.3390/met14020144

Academic Editor: Antonio Mateo

Received: 11 November 2023
Revised: 22 December 2023
Accepted: 4 January 2024
Published: 24 January 2024

1. Introduction

As a representative of the third generation of advanced high-strength steel, medium-Mn steels have shown prospective applications in the automotive industry and are considered appropriate because of their cost advantages and superior mechanical properties [1–3]. It was confirmed that the excellent mechanical properties of traditional medium-Mn steel are mainly attributed to the microstructural characteristics which are composed of ferrite and retained austenite [4,5], where a large amount of ferrite is conducive to dislocation slip, consequently improving the ductility [6]. Further, an adequate amount of RA provides the transformation-induced plasticity (TRIP) effect under tensile stress. An effective TRIP effect can improve work-hardening behavior and high tensile strength while minimizing local stress concentrations and providing high elongation [7,8]. It is well known that the TRIP effect is sensitive to RA characteristics, such as volume fraction, morphology, size, and mechanical stability. Thus, utilizing alloy design concepts and process routes to optimize RA characteristics has become an appealing topic in governing the mechanical property of medium-Mn steel.

The conventional treatment process for medium-Mn steel usually involves an intercritical annealing (IA) process, during which austenite reverse transformation (ART) occurs and its stability is improved by partitioning C and Mn elements into austenite, resulting in some austenite retained at room temperature [9]. A series of findings on the

Fe-(5–7)Mn-(0.1–0.2)C (wt.%) ternary alloy systems have been reported [10,11], indicating that an increase in C and Mn content can achieve excellent mechanical properties by increasing the volume fraction of RA. Recently, some steels with highly comprehensive mechanical properties have been developed. For instance, Cai et al. [12] achieved a UTS of 1007 MPa with a total elongation (TEL) of 65% in cold-rolled Fe-11Mn-4Al-0.2C (wt.%) steel, which was attributed to a discontinuous TRIP effect involving stress relaxation and transfer during deformation. Song et al. [13] developed a Fe-7.75Mn-2.78Al-0.52C (wt.%) steel which was processed by cold-rolling and characterized by a good combination of 1090 MPa UTS and 56.3% TEL. This was attributed to the TRIP/TWIP effect, high dislocation density, and high fraction of RA. However, adding a large amount of Mn can lead to serious difficulties in the continuous casting, rolling, and annealing processes, such as segregation, hot cracking, and high sensitivity to process parameters, resulting in the limited progress of industrial practice and commercial applications [14].

Thus, various alloy design concepts and process routes have been introduced to meet higher requirements. Notably, it has been proved that after ART treatment and followed by a quenching and partitioning (Q&P) treatment, the thermal and mechanical stability of RA can be effectively improved, leading to sustainable work hardening and good ductility [9]. In addition, rapid heating and cyclic quenching (CQ) has been also introduced. Liu et al. [15] studied the microstructural evolution and corresponding mechanical properties of Nb-Mo micro-alloyed medium-Mn steel subjected to novel CQ-ART. It was found that the stability of RA was significantly improved with an increasing number of cyclic quenching, and the optimum comprehensive properties were a UTS of 838 MPa, a TEL of 90.8%, and a PSE of 76.1 GPa%. As a potential process, warm rolling was applied to medium-Mn steel to further improve its mechanical properties, and/or the simple traditional three-stage processes were applied including hot rolling, cold rolling, and ART annealing [16]. When subjected to ART-annealing first and then warm rolling at 650 °C (between A_{c1} and A_{c3}) with different rolling reductions, it was found that the dual phase microstructure of ferrite and RA in 0.1/0.2C-5Mn steel was further refined without the loss of much RA, thereby, enhancing its mechanical properties [17]. Although these routes are promising technologies for improving the mechanical properties of medium-Mn steel, their application is restricted by the existing industrial production lines and costs. For application in the continuous-annealing process, the addition of Al was considered for medium-Mn steel to meet the heat treatment condition with a high temperature and a short holding time [18]. When annealing at a higher temperature, a desirable fraction of austenite with reasonable stability can be obtained by suppressing cementite formation. Further, it was verified that for every 1 wt.% addition of Al, the density of the steel can be reduced by around 1.1%, promoting lightweight steel.

In light of the grain refinement, it is beneficial to enhance mechanical properties. Micro-alloying technology has become an effective way to design a new type of medium-Mn steel. Adding 0.15 wt.% of Ti to 5 wt.% Mn steel can precipitate a large number of nano-sized TiC, effectively inducing grain refinement [19]. However, Park et al. [20] added different contents of Nb, Ti, and V into medium-Mn steel to investigate the effect of micro-alloying and found that the formation of MC carbides increased the strength of the steel, but the TEL decreased due to precipitation hardening. Bi et al. [21] also indicated that a higher V addition increased the YS but decreased the ductility, which is caused by a higher quantity of V_4C_3 precipitates. In fact, the precipitation of carbonitrides also has a considerable impact on the stability of RA. Cai et al. [22] reported that 6.5 wt.% Mn steel containing 0.22 wt.% of Mo and 0.05 wt.% of Nb exhibited slightly higher ductility and YS values due to the increased volume fraction and mechanical stability of RA, while Hu et al. [23] proposed that the consumption of C by carbides decreases austenite stability.

The objective of the study was to develop medium-Mn steels with excellent mechanical properties that are suitable for actual production by combining traditional ART processes and micro-alloying technology. Thus, three novel steels with different V contents were

designed to explore the influence of V micro-alloying on the microstructure evolution, mechanical properties, and RA stability.

2. Experiments

A total of 20 kg of medium-Mn steel ingots with a nominal composition of 0.2C-5Mn-0.3Si-2.2Al-0/0.05/0.15V (wt.%) were fabricated by a vacuum induction melting method and cut into 30 mm thick slabs. The steels without V, and with 0.05 and 0.15 (wt.%) V, are named FV, LV, and HV steels, respectively. Subsequently, the slabs are hot rolled into 3 mm thick sheets at 1150–950 °C. After air cooling, a batch annealing treatment at 780 °C for 3 h was carried out in order to prevent edge cracks from frequently forming during cold rolling [24]. Finally, the hot-rolled sheets were pickled and cold-rolled into 1.6 mm thick strips. The chemical compositions of the strips were determined and are given in Table 1. Using an AccuPyc II 1340 fully automatic true density tester to measure the density of experimental steel, it was found that the addition of 2.2–2.3 wt.% of Al reduced the density to 7.5-7.6 g/cm^3. The three steels were intercritically annealed at 730 °C for 3 min, and then water quenched to ambient temperature. Dog-bone-shaped tensile samples of 12.5 mm width and 50 mm gauge length were machined parallel to the rolling direction. The tensile test was performed at room temperature on an MTS Alliance RT 30 testing machine with a constant 2 mm·min^{-1} cross-head velocity, and the data were the average of three samples. The variation process of RA volume fraction with tensile strain was measured using an X-ray stress apparatus with micro-electronic universal testing. The schematic diagram of the instrument, sample size, and experimental method are in Ref. [25].

Table 1. Chemical composition (wt.%) of experimental steel.

Steel	C	Mn	Al	Si	V	Fe
FV	0.20	5.05	2.12	0.26	-	Bal.
LV	0.21	4.84	2.30	0.25	0.04	Bal.
HV	0.19	5.14	2.19	0.26	0.13	Bal.

The microstructures of the samples were analyzed by Smart Lab X-ray diffraction (XRD) using a Zeiss Sigma 300 field emission scanning electron microscope (SEM) equipped with electron backscattered diffraction (EBSD) and JEM-2100 F transmission electron microscope (TEM). SEM specimens were etched with a 4 vol% nital solution after mechanical polishing, while the specimens for XRD and EBSD were electro-polished in a mixed solution of 80% glacial acetic acid and 20% perchloric acid at ~16 V for 2 min. Phase identification and grain characteristics were measured by EBSD, and the acceleration voltage and step size were 20 kV and 0.06 μm, respectively. The RA fractions and average C concentrations in RA were quantified via XRD (Cu K_α radiation, scan rate of 10°·min^{-1}, diffraction angle (2θ) of 40–100°) based on the integral intensity and austenite lattice parameter of the diffraction peaks. The method can be found in Refs. [26,27]. For the TEM analysis, thin foil samples with a diameter of 3 mm were mechanically polished to <60 μm, and followed by twin-jet electro-polishing in a mixed solution of 10% perchloric acid and 90% ethanol at −40 °C. The characteristics of precipitates were observed in detail using TEM on carbon extraction replicas.

3. Results and Discussion

3.1. Evolution of Microstructure and Mechanical Properties after V Microalloying

3.1.1. Microstructure

Figure 1 presents the representative SEM micrographs of the three steels annealed at 730 °C. The microstructural constituents of FV steel were composed of intercritical ferrite (α-ferrite) and RA, accompanied by a certain amount of fibrous δ-ferrite bands extending along the rolling direction. By comparison, it was found that the microstructure of LV steel was more uniform and contained a slightly lower δ-ferrite content, which may be

related to its higher C content [28]. The δ-ferrite is formed during the early stage of the solidification of steel, which is difficult to change to austenite and then α-ferrite [29]. Sun et al. [30] reported that the presence of δ-ferrite in medium-Mn steel would easily induce the initiation of voids and micro-cracks at the interfaces of δ-ferrite and deteriorate the mechanical properties. In the subsequent ART process, due to the rather high stored energy in the heavily cold deformed structure, reverted austenite is readily recrystallized [31], and RA can be obtained at ambient temperature.

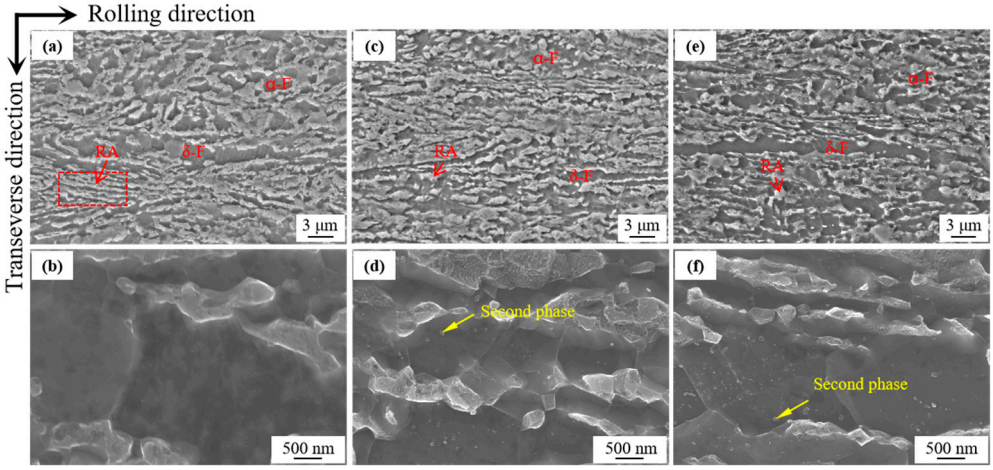

Figure 1. SEM analysis of the microstructure of experimental steels with different V contents after IA: (**a**,**b**) FV steel, (**c**,**d**) LV steel, and (**e**,**f**) HV steel.

In the α-ferrite+RA region, it was clear that most of the RA grains were relatively homogeneously distributed in the α-ferrite matrix. Because of the lower IA temperature and short holding time, some RA grains were distributed in an equiaxed shape. Other RA grains were forcibly interrupted before they could grow up and retain the lamellar morphology, similar to the lath martensite of cold-rolled strip, which exists along with α-ferrite, forming a kind of micro-laminated microstructure, as shown in the dotted box in Figure 1a. From magnified microstructures, a large number of second-phase precipitation appeared in the matrix of the V-added steels, as indicated by the arrows in Figure 1d,f, while no obvious second-phase could be seen in the matrix of FV steel (Figure 1b). Since the IA temperature was 730 °C, it could be speculated that the precipitates should be VC particles. It should be noted that the carbide distribution density of 0.13 V is higher than that of 0.04 V.

The RA characteristics and second phase of the three steels were analyzed by TEM in detail (Figures 2 and 3). The TEM bright-field micrographs in Figure 2a show that the lath-like α-ferrite was present in FV steel, and an equiaxed RA grain with a size of 0.28 μm was observed at the grain boundary of α-ferrite. Figure 2b and c illustrate the dark field image and selected area electron diffraction (SAED) of RA, respectively. After adding 0.04 wt.% V, no significant changes were observed in the morphology of α-ferrite, as shown in Figure 2d–e, but relatively large differences existed between FV and LV steel in terms of morphology and size. For LV steel, a lath-like and equiaxed micro-morphology of RA was present, and the lath length and width of lath-like RA in LV steel were measured to be 1.32 μm and 0.33 μm, which indicated that the size of RA in LV steel increased greatly.

Figure 2f–h shows the bright and dark field image of HV steel, and the SAED of $(110)_\gamma$ was used to recognize RA, which showed clear twin reflections, indicating that there was an annealing twin in the RA grain. Regarding HV steel, it is shown that the equiaxed RA and α-ferrite were distributed, in which the size of RA was in the range of 0.33–0.58 μm. This result reflected that the further increase in V accelerated the formation of an equiaxed microstructure and was beneficial to the grain refinement of RA. Moreover, numerous particles were found inside the α-ferrite grains of HV steel, and the EDS result presented in Figure 2i shows that V was enriched in these particles, which can be inferred

to be VC carbide. Figure 2j shows the picture under the high-angle annular dark-field (HAADF), and it clearly highlights a layered microstructure consisting of lathy RA adjacent to α-ferrite, which indicates that the martensite interface served as the nucleation sites for reverted austenite formation. As shown in Figure 2k,l, the corresponding STEM-EDS distribution diagrams show that Mn tended to be enriched in RA and Al tended to be enriched in α-ferrite, indicating that there was an obvious Mn and Al partition between RA and α-ferrite within the intercritical region.

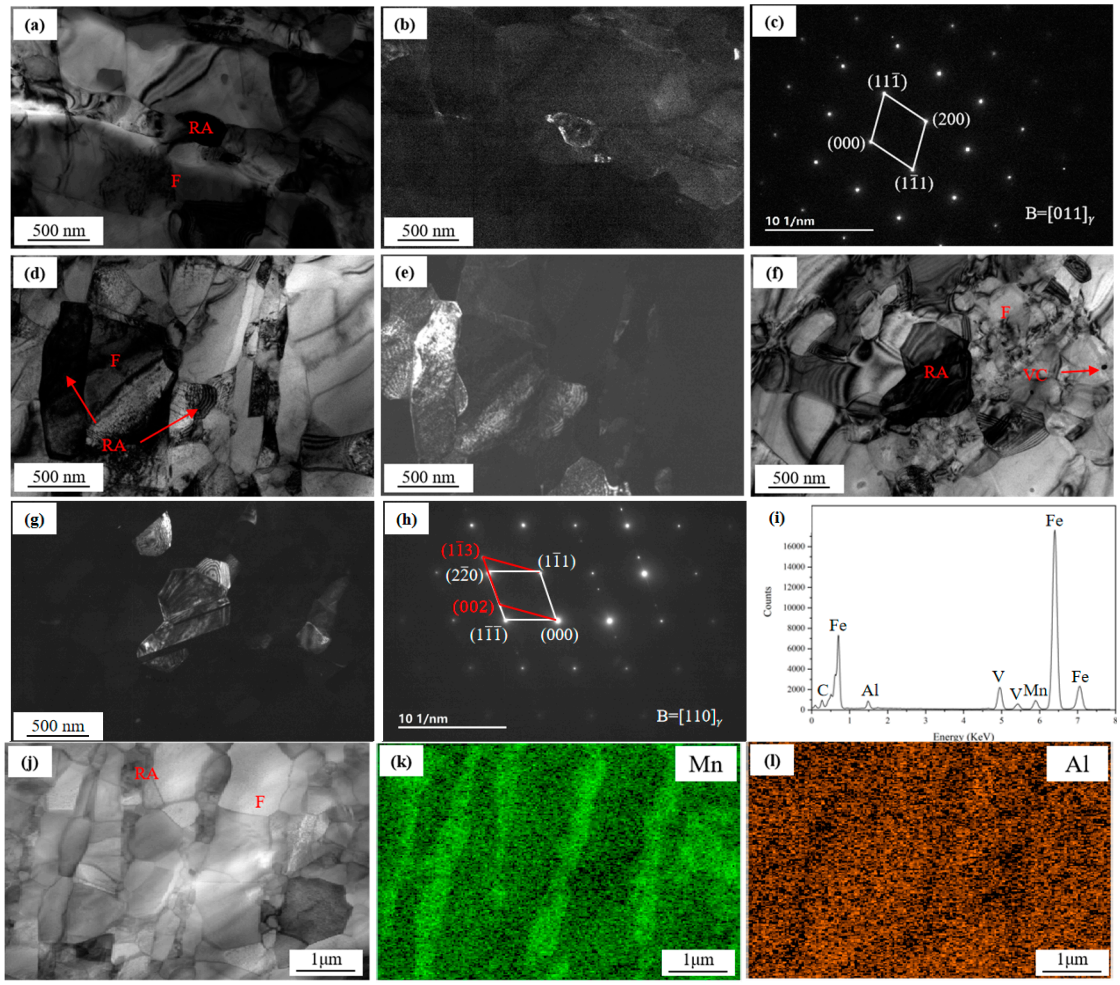

Figure 2. TEM analysis of experimental steel after IA: (**a**) bright-field micrograph of FV steel, (**b**) dark-field micrograph of RA in FV steel, (**c**) SAED pattern of RA in FV steel, (**d**) bright-field micrograph of LV steel, (**e**) dark-field micrograph of RA in LV steel, (**f**) bright-field micrograph of HV steel, (**g**) dark-field micrograph of RA in HV steel, (**h**) SAED pattern of RA in HV steel, (**i**) EDS spectroscopy of V carbide in HV steel, and (**j**–**l**) HAADF and EDS maps of LV steel.

To further analyze the characteristics of the second phase, the carbon extraction replica samples of V-added steels after annealing were analyzed by TEM, as shown in Figure 3a. In the case of LV and HV steels, a large amount of second-phase particles were spherical. The SAED analysis of the large particles is presented in Figure 3c. The results showed that they had an FCC structure, which further confirmed that the precipitated phase was VC. The mean planar intercept diameter of VC was conducted based on several TEM images, and the statistical results are shown in Figure 3d. It can be seen that the average size of precipitates in LV steel was ~30 nm, while that in HV steel was ~38 nm, indicating a remarkable increase. Thus, it can be concluded that, apart from the volume fraction, an increase of V is capable of promoting the growth of VC during IA. In addition to the VC observed in LV and HV steels, numerous particles with a diameter of approximately

50 nm were detected in the TEM analysis of FV steel as shown in Figure 3e, which is identified as cementite by SAED in Figure 3h. Previous research indicates that the austenite nucleates at the cementite/ferrite interface, and cementite is generally replaced by reversed austenite [32,33]. In Figure 3f, it can be seen that the cementite retained in FV steel was surrounded by austenite, which reflects that the austenite is formed around the cementite. Further, due to the dissolution of cementite controlling the growth and volume fraction of austenite, the incomplete dissolution of cementite in FV steel had a negative impact on the volume fraction and stability of obtaining reversed austenite. It is worth noting that the cementite was not observed in LV and HV steels. This absence may be attributed to the inhibitory effect of V addition on cementite formation. The precipitation temperature of cementite in FV, LV, and HV steels was calculated using the Thermo-Calc software (Thermo-Calc version 2019a) [34], resulting in values of 664.9 °C, 663.6 °C, and 658.0 °C, respectively. It is evident that the formation temperature of the cementite decreased with the increased V content, indicating that V reduced the phase stability of the cementite.

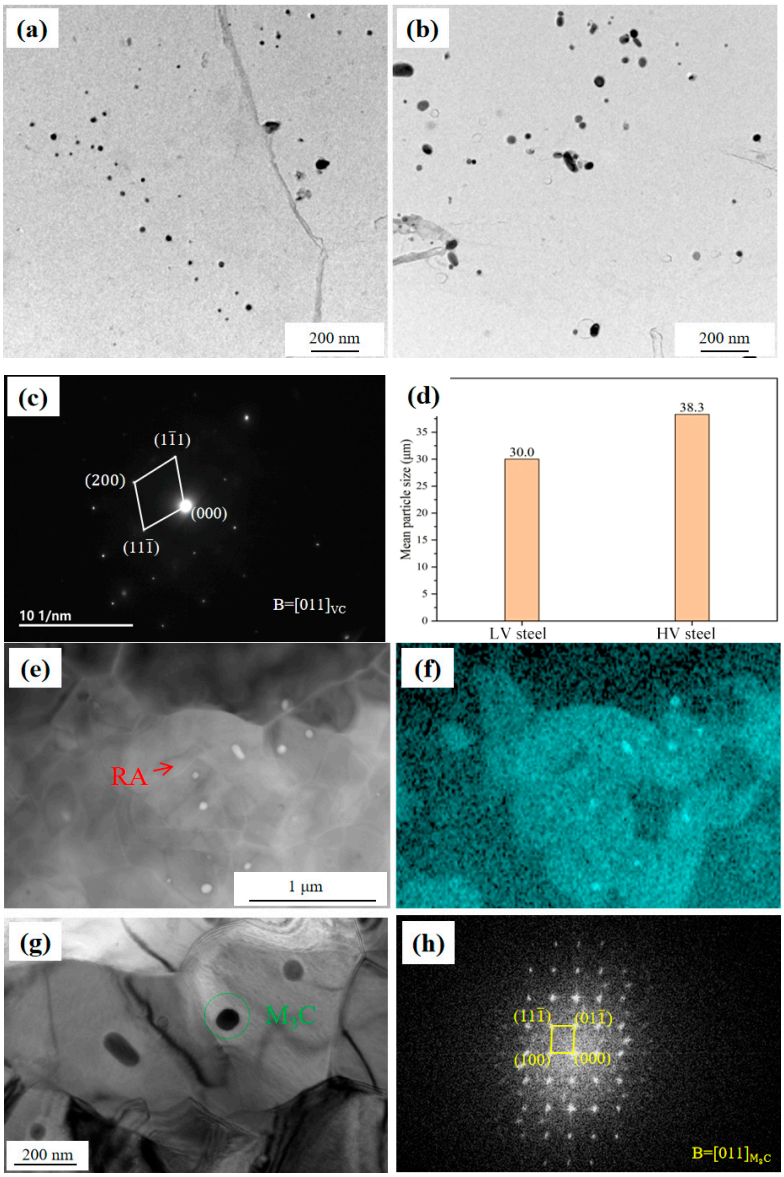

Figure 3. TEM analysis of carbides after IA: (**a**) TEM micrographs in LV steel, (**b**) TEM micrographs in HV steel, (**c**) SAED pattern of VC, (**d**) average particle size of VC in LV steel and C, (**e**,**f**) HAADF and EDS maps of FV steel, (**g**) bright-field micrograph of FV steel, and (**h**) SAED pattern of cementite in FV steel.

The microstructures characterized by EBSD are shown in Figure 4. In the micrographs (Figure 4a–c), the RA phase was green-colored and the ferrite phase was red-colored. It is clear that the RA was primarily located in the boundary regions or triple junctions of the α-ferrite phase, with only a small amount of RA appearing inside the α-ferrite in FV steel, and its size was smaller than the former. Figure 4j illustrates the average size of the RA and α-ferrite in the three steels, and the results show that the addition of the V element effectively restricted the growth of α-ferrite, promoting the refinement of α-ferrite grains. The α-ferrite size decreased from 1.328 μm to 0.910 μm with the addition of 0.04 wt.% of V, followed decrease to 0.826 μm when the content of V increased to 0.13 wt.%. However, the size of RA first increased from 0.424 μm to 0.520 μm, then tended to decrease with further increases in the V element. Luo et al. [35] revealed through experiments and simulations that the nucleation of the intercritical austenite only involves partition and diffusion of carbon due to the very short time, but its growth kinetics are dominated by the diffusion of Mn in both the austenite and α-ferrite phases, particularly in the austenite phase. Varanasi et al. [36] provided evidence of Mn migration to austenite through grain boundary (GB) diffusion, GB migration, and dislocation pipe diffusion. Further, they reported that the grain size of austenite nucleated at high-angle grain boundaries (HAGB) is considerably greater compared to the austenite formed at a low angle grain boundaries (LAGB), due to the absence of bulk manganese diffusion and predominant GB diffusion. Thus, the GB distributions of the three steels are presented in Figure 4d–f, where the LAGB (2–5°), medium angle grain boundary (MAGB, 5–15°), and HAGB (>15°) are depicted as red, green, and blue lines, respectively, and the variations of various GBs proportion are given in Figure 4k. It is obvious that as the V content increased, the proportion of HAGBS gradually decreased, while the proportion of LAGBS increased. Based on this, the addition of V inhibited the growth of austenite. However, although the proportion of HAGB in LV steel was weaker than that of FV steel, the relatively smaller size of α-ferrite led to an increase in the total density of various GBs, which is conducive to the diffusion of Mn, thereby promoting the growth of austenite. In addition, the diffusion coefficient of C in the three steels was calculated using the Diffusion Module (DICTRA) in Thermo-Calc software (Thermo-Calc version 2019a) [34], which were 5.538×10^{-13}, 5.604×10^{-13}, and 5.433×10^{-13} m^2/s. These results showed that the nucleation ability of austenite also exhibited a similar trend to grain size, indicating that austenite in LV steel was more prone to nucleation. This phenomenon can be regarded as another reason why LV steel shows a much higher RA fraction than FV and HV steels, as shown in Figure 4a–c.

The volume fraction of RA in annealed samples was determined by the XRD analysis, in which Figure 5a shows the XRD pattern, and the measured RA fraction is summarized in Figure 5b. The RA content in the LV steel had a maximum of ~32.6 vol.% after annealing at 730 °C, while that in the other two experimental steels, both ranged from 22% to 23%. This result does not show a significant linear relationship. In general, the fraction of RA depended on the amount of austenite formed during the IA treatment, as well as the composition of intercritical austenite. By comparing the thermodynamic calculation of the phase fraction of the austenite in experimental steels by the Thermo-Calc software [34] in Figure 6, it can be seen that when annealing at 730 °C, there was a small difference in the intercritical austenite content of the equilibrium state of the three steels, ranging from 40.4% to 44.7%. However, the residual cementite in FV steel indicates that the reverse transformation of austenite is relatively slow, and it is speculated that the critical austenite content transformed is lower than that of the other two types of steel. Further, the retention of RA also depends on the thermal stability of intercritical austenite, which is mainly related to its alloy composition. Since the duration of IA is short, it is expected that C will be mainly partitioned, while Mn can only undergo short-range diffusion. The calculated carbon content in the intercritical austenite after the equilibrium of the three sheets of steel was 0.441 wt.%, 0.486 wt.%, and 0.399 wt.%, respectively, indicating that the intercritical austenite in LV steel had the highest thermal stability and was less prone to transformation during subsequent cooling processes. EBSD was used to characterize the distribution of

geometrically necessary dislocations (GNDs), as shown in Figure 4g–i. It can be observed that the GND in the experimental steel was distributed along grain boundaries or near RA, and the amount of GNDs increased significantly with V content, especially in HV steel. The reason may be that the increase in precipitation leads to the obstruction of recrystallization and recovery, causing more GNDs to be retained. After deformation, XRD analysis was performed on the tensile samples near the fracture surface, as shown in Figure 5c. One can see the peaks corresponding to austenite in the XRD pattern of the three steels disappeared, indicating that almost all austenites underwent stress-induced martensitic transformation.

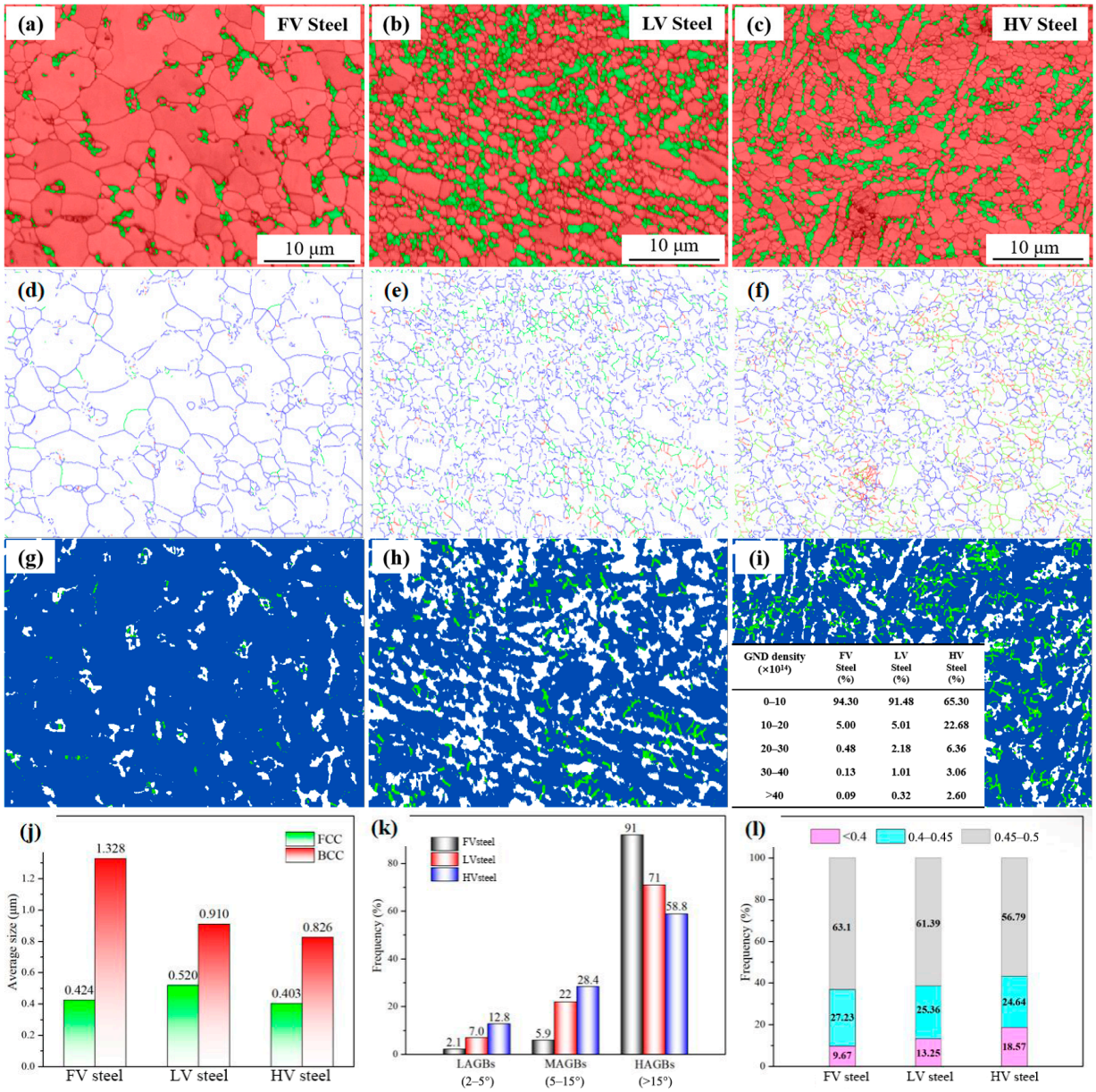

Figure 4. EBSD analysis of experimental steel after IA: (**a**–**c**) phase distribution diagram in experimental steels. Red and green colors denote the bcc and fcc phase regions, respectively. (**d**–**f**) Grain boundary distribution in experimental steels. Red, green, and blue colors denote LAGB, MAGD, and HAGB, respectively. (**g**–**i**) Geometrically necessary dislocations distribution in experimental steels. (**j**) Average size of ferrite and RA, (**k**) GBs proportion, and (**l**) Schmidt factor (SF) in experimental steels.

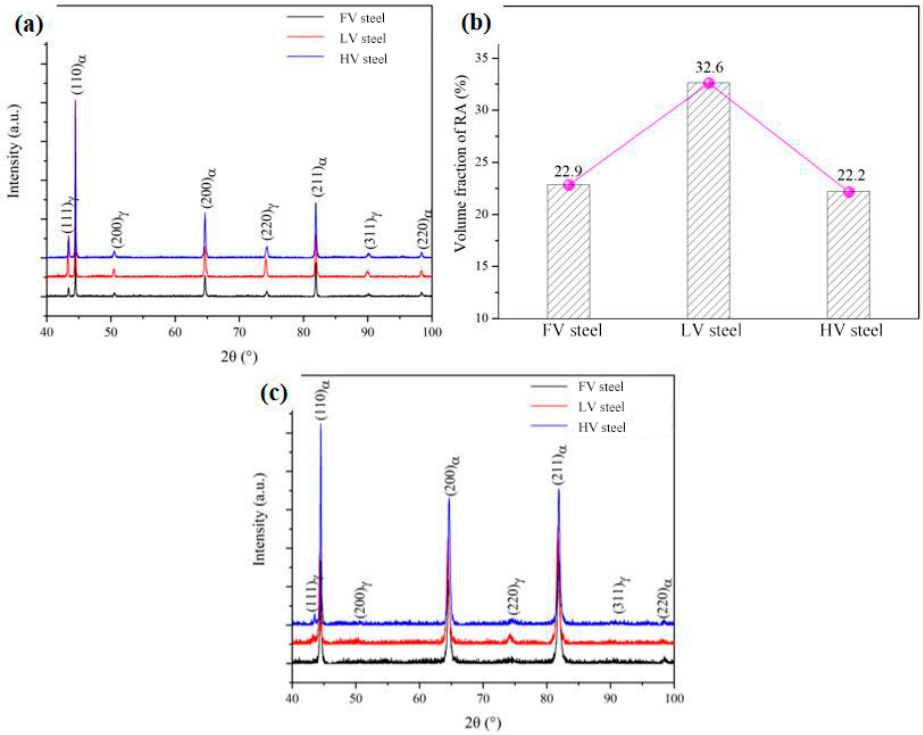

Figure 5. XRD pattern of experimental steel after IA: (**a**) before tensile test, (**b**) volume fraction of RA, and (**c**) after tensile test.

Moreover, based on the XRD results, the carbon content in RA was calculated as 1.17 wt.%, 1.31 wt.%, and 1.14 wt.% according to the austenite lattice parameter, which is in good agreement with the results of the theoretical calculation, showing a relationship of $C_B > C_A > C_C$. A higher C content in LV steel is beneficial for improving the austenite stability. Additionally, the Schmidt factor (SF) was also statistically used for subsequent analysis of austenite stability, as shown in Figure 4l. It can be seen that as the V content increased, the proportion of RA grains having an SF value greater than 0.45 decreased, illustrating that more RA grains did not transform into martensite during the deformation process due to their unfavorable orientations to the loading direction [36]. In this regard, RA in HV steel can exhibit high stability.

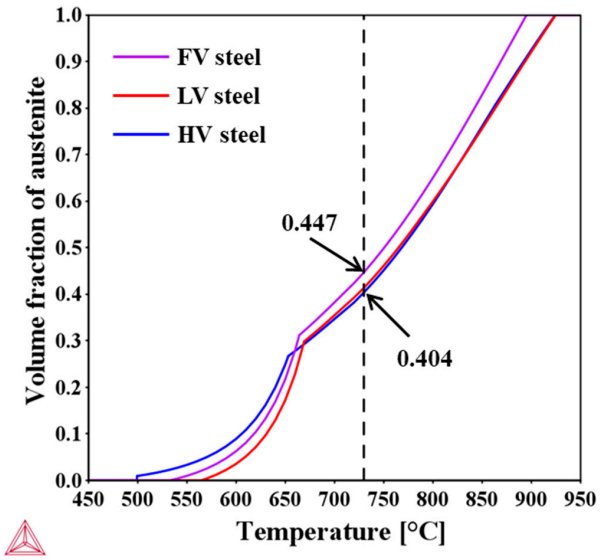

Figure 6. Equilibrated phase fraction of austenite in experimental steels.

3.1.2. Mechanical Properties

Figure 7 shows the engineering stress-strain curves of three experimental steels treated with ART. The three steels exhibit similar deformation behavior, with obvious yield points on the curves, followed by gradual work hardening with TRIP. After necking, slight elongation occurs and then fractures due to plastic strain localization. The YS, UTS, TEL, and PSE of the investigated steels are summarized in Table 2. It can be seen that the FV steel without the V element exhibited a YS of 719 MPa, yield stress UTS of 940 MPa, and TEL of 39.5%. As V content increased, the YS gradually increased to 788 MPa, while TEL decreased to 35%. Similar changes in TEL and PSE are observed in Table 2, with UTS and PSE first increasing and then decreasing with an increase in V content. The PSE for the three steels was greater than 30 GPa%, and LV steel exhibited the highest value of PSE, characterized by optimum mechanical properties.

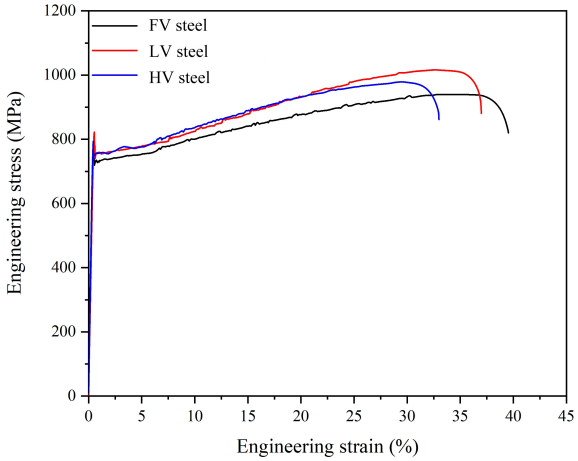

Figure 7. Engineering stress-strain curve.

Table 2. Mechanical properties of experimental steels with different V contents after IA.

Steel	YS (MPa)	UTS (MPa)	TEL (%)	PSE (GPa%)
FV	719	940	39.5	37.1
LV	746	1020	37.0	37.7
HV	788	987	35.0	34.5

In terms of the YS, it gradually increased with the increase of V content, which was first related to the precipitation strengthening effect generated by the precipitation of nanoscale VC through pinning dislocation movement. In addition, the three types of experimental steels underwent IA to form soft α-ferrite, and the softening effect was related to the low yield strength of the samples. It is evident in Figure 4j that an increase in V content restricted the growth of α-ferrite, and an increase in the contribution of fine grain strengthening led to an increase in the YS. Moreover, after annealing at 730 °C, some hard-phase fresh martensite was formed in the process. The increase in GND in steel observed in Figure 4g–i was also beneficial for the improvement of yield strength. Regarding the UTS and TEL, it is well known that the addition of V to LV and HV steels can contribute to the UTS through precipitation hardening and fine grain strengthening, while precipitation hardening reduces plasticity. In this work, it is obvious that the negative effect of precipitation strengthening on plasticity is stronger than the positive effect of grain refinement, resulting in the TEL showing a similar tendency. However, it is worth noting that compared to LV steel, the UTS of HV steel decreases, indicating that these strengthening mechanisms do not seem to be the main factors for obtaining a high UTS. In TRIP-aided steels, the mechanical properties are profoundly affected by the TRIP effect, which depends on the amount and stability of RA. There was no significant correlation between the amount of RA and the TEL. Hence, the deformation mechanisms and austenite stability will be further elucidated.

3.2. Work-Hardening Behavior and Austenite Stability

The stability of austenite can be reflected by the work hardening rate (WHR) during the tension process. Thus, the true strain-stress plots and work hardening curves of the three annealed samples are presented in Figure 8. The WHR evolution can be divided into three stages. All decreased sharply at first then increased with fluctuations, and finally decreased again in the third stage. In the S1 stage, the rapid decrease in the WHR corresponded to the elastic deformation stage of the true strain-stress curves, which is mainly associated with the yield deformation of the soft ferrite phase [37]. Next, numerous peaks were present in the S2 stage, which is ascribed to the TRIP active effect. It is worth noting that the WHR remained relatively stable in the early stage, and then fluctuated considerably with the increase of true strain. This is because there is competition between the strength increase effect caused by the TRIP effect of RA and the softening effect of ferrite deformation. As the deformation continues, the progressive TRIP effect of RA leads to an increase in strength, overcoming the softening effect of ferrite deformation [38]. The strain in the S2 stage of FV and LV steels both persisted at >0.27, which was higher than that of HV steel, indicating that the coordinated influence of the TRIP effect and ferrite deformation in both steels was greater than that in HV steel. Finally, the TRIP effect of austenite was depleted and unable to compensate for the failure of large plastic deformation within the microstructure, resulting in a decrease in the WHR.

The transformation from austenite to martensite during deformation introduces phase transformation strengthening and plasticity enhancement. For this reason, in addition to ensuring a high content, the austenite must have appropriate stability to ensure the TRIP effect persists, achieving the simultaneous increase of strength and plasticity. It is common knowledge that austenite stability depends primarily on chemical composition, grain size, morphological characteristics, and crystallographic orientation [25]. It can be seen from earlier results that there are differences in RA characteristics among the three experimental steels. For example, although LV steel contained the highest C content in RA, its size and SF value representing crystallization characteristics did not reflect better stability than FV and HV steels. Therefore, it is difficult to comprehensively compare the stability of RA in the three steels based on their microstructure characteristics.

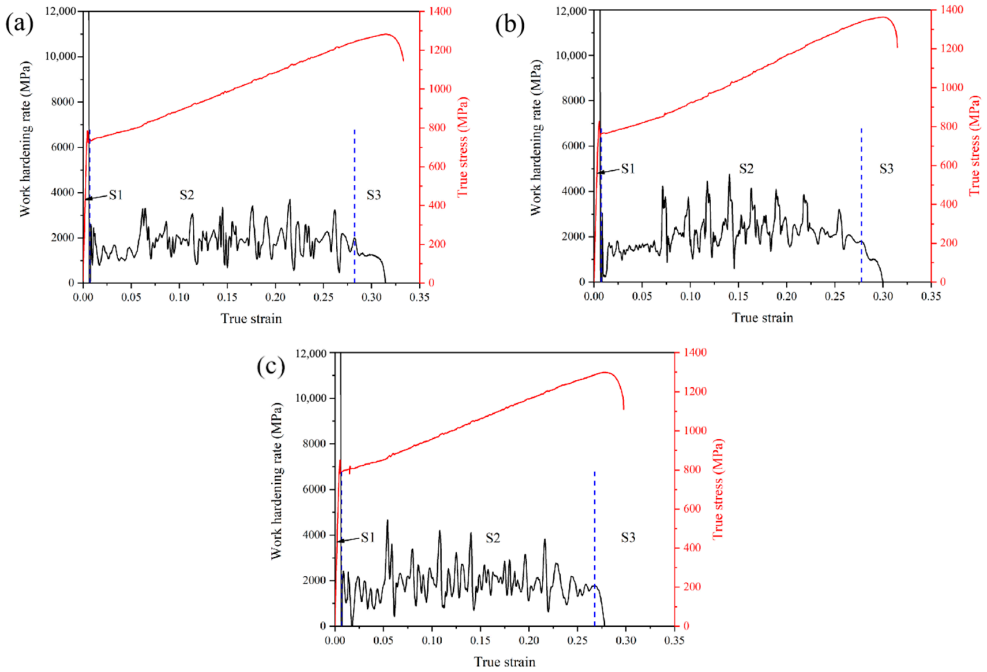

Figure 8. Work hardening rate and true stress-true strain curves of experimental steel after IA: (**a**) FV steel, (**b**) LV steel, and (**c**) HV steel.

In order to quantify the differences in RA stability among three experimental steels, the RA volume fraction at different strains was detected using a micro-electronic universal testing machine and in situ X-ray stress apparatus instrument. As shown in Figure 8, when the engineering strain was less than 4–5%, the RA content of the three experimental steels was relatively stable, consistent with the RA content before tension, maintained at 26.2%, 34.0%, and 23.1%, respectively. Then, the RA fraction gradually reduced and this contributed to an active TRIP effect. It should be noted that compared to LV steel, the RA content in other steels both showed a trend of a first rapid decrease and then a slow decrease. When the engineering strain exceeded 25%, the RA content in both steels was less than 2%, and there was no significant change in subsequent deformation, indicating that the rest of the austenite was not able to proceed with martensitic transformation. However, for LV steel, the decreasing trend of the RA fraction was lower than that of FV and HV steels, and the decreasing process continued with the increased engineering strain. When the strain increased to 37.5%, the RA content decreased to 3%. This suggests that RA grains with different stability underwent martensitic transformation successively throughout the entire deformation process, resulting in a more durable TRIP effect. Furthermore, Figure 9 also determines that the corresponding engineering stress at the beginning of RA transformation were 722 MPa, 778 MPa, and 794 MPa, which were basically consistent with the YS value, except that the results for LV steel were slightly higher than its YS value. This demonstrates that RA undergoes martensitic transformation after yielding, and a higher stability of RA in LV steel requires a higher stress to activate the TRIP effect. These results are evidence that austenite is not related to the increase in YS and also prove that the TRIP effect can significantly improve strain-hardening ability.

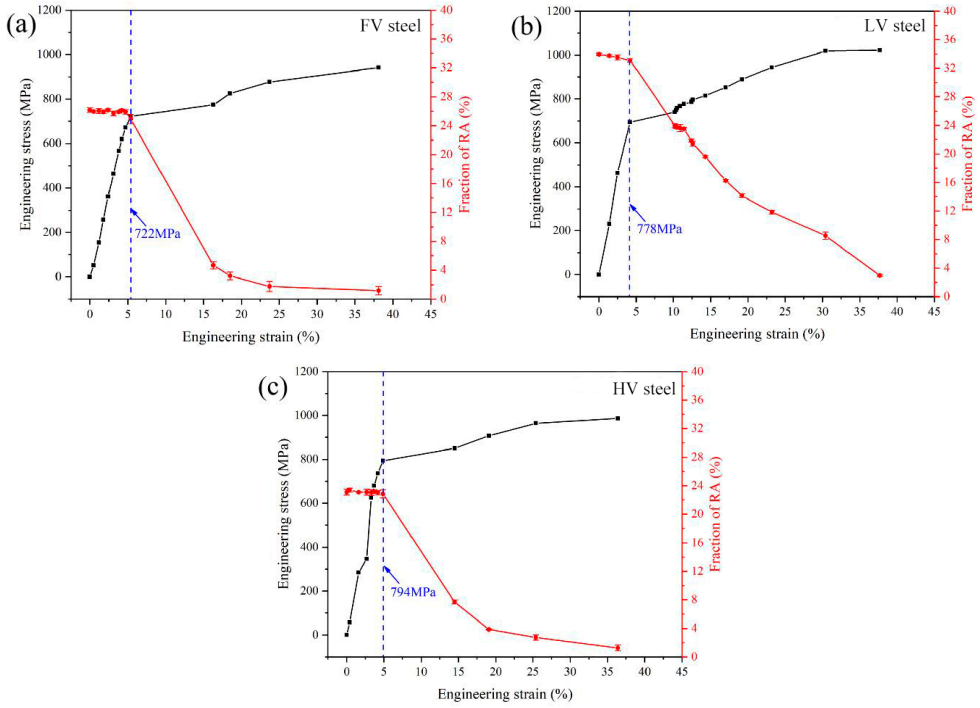

Figure 9. RA amount and engineering stress vs. engineering strain of experimental steel after IA: (**a**) FV steel, (**b**) LV steel, and (**c**) HV steel.

Generally, the mechanical stability of austenite can be calculated by the following equation [39]:

$$k\varepsilon = -\ln(V_\gamma / V_{\gamma_0}) \quad (1)$$

where V_{γ_0} is the initial RA content; V_γ is the content of RA at true strain ε; and k reflects the mechanical stability of RA. Generally, the higher the k value, the lower the driving force required for the transformation of RA into martensite, corresponding to a lower stability.

Figure 10 describes the linear fitting process between ε and $-\ln(V_\gamma/V_{\gamma 0})$ to determine the k value. It is obvious that the RA in LV steel has the highest stability (k = 8.03), and stress-induced martensitic transformation can still occur under high strain, and more RA can be retained after tensile testing. In fact, the film type RA was observed in LV steel after the tensile test, as shown in Figure 11. Due to the high stability of the film type RA, the austenite was retained after tensile testing. Furthermore, the granular area was observed and had the Kurdjumov-Sachs orientation relationship with the austenite according to the SAED pattern. Moreover, a high density of dislocations was found in the granular area, providing further evidence of it being martensite. In contrast, the k values of FV and HV steels were comparable, suggesting that there was no significant difference in the stability of RA between the two steels, both of which are lower than that of LV steel. The consistency of the C concentration in RA and the k value demonstrates that the C content in RA is a critical factor governing the mechanical stability of RA. These results reveal that the largest amount of RA and appropriate stability result in LV steel exhibiting outstanding UTS. However, it is worth noting that the persistent TRIP effect and grain refinement did not effectively improve the plasticity of the experimental steel, but rather slightly decreased the elongation. Therefore, we may infer that the above two plasticizing mechanisms cannot offset the negative effect of precipitation hardening on plasticity. With the further increase of V content, the TRIP effect was weakened while precipitation hardening was further strengthened, resulting in a further decrease in the elongation of HV steel, and consequently, the PSE was reduced.

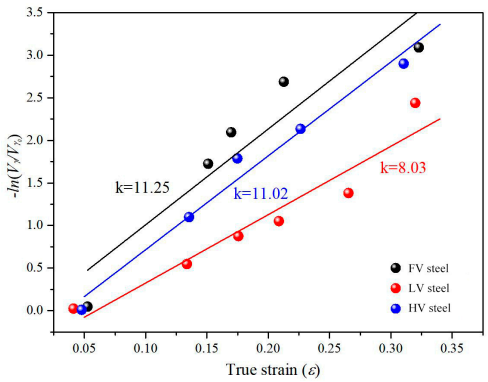

Figure 10. k value of experimental steel after IA.

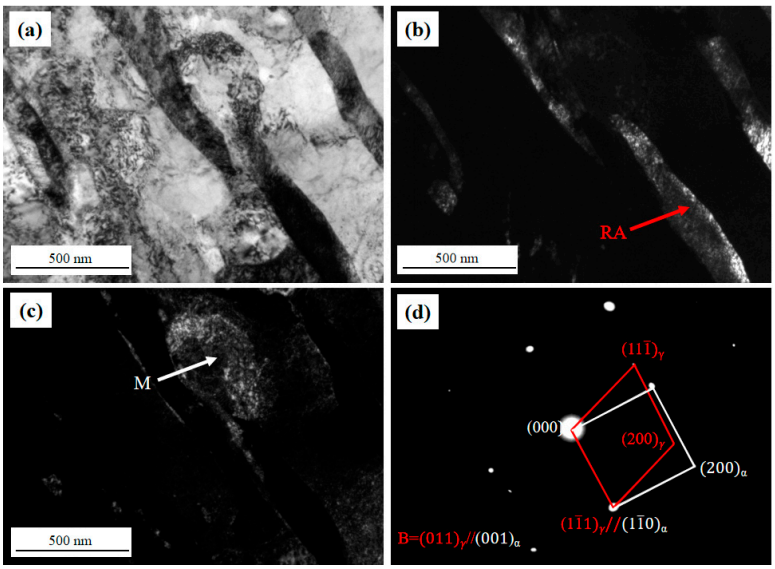

Figure 11. TEM analysis of LV steel after tensile test: (**a**) bright-field micrograph, (**b**) dark-field micrograph of RA, (**c**) dark-field micrograph of martensite, and (**d**) SAED pattern of RA and martensite.

4. Conclusions

The present work conducted a detailed study on the correlation between the mechanical properties and microstructural characteristics of V micro alloyed low-density medium-Mn steel. The findings are as follows:

(1) Cold-rolled medium-Mn steels with different V content were subjected to IA treatment at 730 °C, and their microstructure was similar, consisting of α-ferrite, RA, and δ-ferrite. The outstanding integrated mechanical properties of a YS of 746 MPa, a UTS of 1020 MPa, a TEL of 37%, and a PSE of 37.7 GPa% were obtained for LV steel. This indicates that 0.04 wt.% of V microalloying could improve the strength-ductility balance of medium-Mn steel to a certain extent.

(2) The C content in RA had a more significant impact on the mechanical stability of RA than the size and orientation of RA according to the experimental measurement of the grain size and Schmidt factor.

(3) The addition of the V element led to the precipitation of VC carbides, which not only produced precipitation strengthening but also refined the α-ferrite and resulted in fine grain strengthening, enhancing the strength of the experimental steel. However, the precipitation of VC also caused a decrease in the TEL of the experimental steel, which is not even compensated by the effective TRIP effect produced in LV steel. On the contrary, the TRIP effect of RA had a certain contribution to improving its UTS.

Author Contributions: C.Y.: Investigation, Writing—original draft. N.Z.: Methodology. Y.M.: Formal analysis. W.Z.: Writing—review & editing. Y.H.: Software. L.L.: Supervision. G.Y.: Supervision. All authors have read and agreed to the published version of the manuscript.

Funding: This research was funded by Young Elite Scientists Sponsorship Program by the China Association for Science and Technology (Grant No. YESS20210357) and the National Natural Science Foundation of China (Grant No. 51901124).

Data Availability Statement: The raw data supporting the conclusions of this article will be made available by the authors on request.

Conflicts of Interest: Author Cansheng Yu was employed by the company State Key Laboratory of Vanadium and Titanium Resources Comprehensive Utilization, Pangang Group Research Institute Co., Ltd. The remaining authors declare that the research was conducted in the absence of any commercial or financial relationships that could be construed as a potential conflict of interest.

References

1. Cai, Z.H.; Ding, H.; Xue, X.; Xin, Q.B. Microstructural evolution and mechanical properties of hot-rolled 11% manganese TRIP steel. *Mater. Sci. Eng. A* **2013**, *560*, 388–395. [CrossRef]
2. Xu, Y.B.; Hu, Z.P.; Zou, Y.; Tan, X.D.; Han, D.T.; Chen, S.Q.; Ma, D.G.; Misra, R.D.K. Effect of two-step intercritical annealing on microstructure and mechanical properties of hot-rolled medium manganese TRIP steel containing δ-ferrite. Mater. *Sci. Eng. A* **2017**, *688*, 40–55. [CrossRef]
3. Bai, Y.; Matsui, Y.; Shibata, A.; Tsuji, N. Effect of thermomechanical processing at α + γ two-phase temperatures on microstructure and mechanical property of 5Mn-0.1C-2Si medium-manganese steel. *Mater. Sci. Eng. A* **2019**, *743*, 57–66. [CrossRef]
4. Han, J.; Lee, S.-J.; Lee, C.-J.; Lee, S.; Jo, S.Y.; Lee, Y.-J. The size effect of initial martensite constituents on the microstructure and tensile properties of intercritically annealed Fe–9Mn–0.05C steel. *Mater. Sci. Eng. A* **2015**, *633*, 9–16. [CrossRef]
5. Suh, D.W.; Kim, N.J. Medium Mn transformation-induced plasticity steels: Recent progress and challenges. *Scr. Mater.* **2017**, *126*, 63–67. [CrossRef]
6. Hu, Z.P.; Xu, Y.B.; Zou, Y.; Misra, R.D.K.; Han, D.T.; Chen, S.Q.; Hou, D.Y. Effect of intercritical rolling temperature on microstructure-mechanical property relationship in a medium Mn-TRIP steel containing δ ferrite. *Mater. Sci. Eng. A* **2018**, *720*, 1–10. [CrossRef]
7. Dobrzanski, L.A.; Borek, W. Mechanical properties and microstructure of high-manganese TWIP, TRIP and TRIPLEX type steels. *J. Achiev. Mater. Manuf. Eng.* **2012**, *55*, 230–238.
8. Lee, S.; Lee, S.-J.; De Cooman, B.C. Reply to comments on "Austenite stability of ultrafine-grained transformation-induced plasticity steel with Mn partitioning. *Scr. Mater.* **2012**, *66*, 832–833. [CrossRef]
9. Dong, Y.; Zhang, B.; Zhao, M.M.; Du, Y.; Misra, R.D.K.; Du, L.X. Investigation of austenite decomposition behavior and relationship to mechanical properties in continuously cooled medium-Mn steel. *Mater. Sci. Eng. A* **2022**, *831*, 142208. [CrossRef]

10. Shi, J.; Sun, X.J.; Wang, M.Q.; Hui, W.J.; Dong, H.; Cao, W.Q. Enhanced work-hardening behavior and mechanical properties in ultrafine-grained steels with large-fractioned metastable austenite. *Scr. Mater.* **2010**, *63*, 815–818. [CrossRef]
11. Miller, R.L. Ultrafine-grained microstructures and mechanical properties of alloy steels. *Metall. Mater. Trans. B* **1972**, *3*, 905–912. [CrossRef]
12. Cai, Z.H.; Ding, H.; Misra, R.D.K.; Ying, Z.Y. Austenite stability and deformation behavior in a cold-rolled transformation-induced plasticity steel with medium manganese content. *Acta Mater.* **2015**, *84*, 229–236. [CrossRef]
13. Li, X.; Song, R.B.; Zhou, N.P.; Li, J.J. An ultrahigh strength and enhanced ductility cold-rolled medium-Mn steel treated by intercritical annealing. *Scr. Mater.* **2018**, *154*, 30–33. [CrossRef]
14. Han, D.T.; Xu, Y.B.; Liu, R.D.; Peng, F.; Zou, Y.; Sun, W.H. Improving Mn partitioning and mechanical properties through carbides-enhancing pre-annealing in Mn-reduced transformation-induced plasticity steel. *Scr. Mater.* **2020**, *187*, 274–279. [CrossRef]
15. Liu, C.Q.; Peng, Q.C.; Xue, Z.L.; Yang, C.W. A Novel Cyclic-Quenching-ART for Stabilizing Austenite in Nb–Mo Micro-Alloyed Medium-Mn Steel. *Metals* **2019**, *9*, 1090. [CrossRef]
16. Hui, W.J.; Shao, C.W.; Zhang, Y.J.; Zhao, X.L.; Weng, Y.Q. Microstructure and mechanical properties of medium Mn steel containing 3%Al processed by warm rolling. *Mate. Sci. Eng. A* **2017**, *707*, 501–510. [CrossRef]
17. Zhan, W.; Cao, L.Q.; Hu, J.; Cao, W.Q.; Li, J.; Dong, H. Intercritical rolling induced ultrafine lamellar structure and enhanced mechanical properties of medium-Mn steel. *J. Iron Steel Res. Int.* **2014**, *21*, 551–558. [CrossRef]
18. Suh, D.-W.; Park, S.-J.; Lee, T.-H.; Oh, C.-S.; Kim, S.-J. Influence of Al on the microstructural evolution and mechanical behavior of low-carbon, manganese transformation-induced-plasticity steel. *Metall. Mater. Trans. A* **2010**, *41A*, 397–408. [CrossRef]
19. Han, Y.; Shi, J.; Xu, L.; Cao, W.Q.; Dong, H. Effects of Ti addition and reheating quenching on grain refinement and mechanical properties in low carbon medium manganese martensitic steel. *Mater. Des.* **2012**, *34*, 427–434. [CrossRef]
20. Park, T.M.; Kim, H.-J.; Um, H.Y.; Goo, N.H.; Han, J. The possibility of enhanced hydrogen embrittlement resistance of medium-Mn steels by addition of micro-alloying elements. *Mater. Charact.* **2020**, *165*, 110386. [CrossRef]
21. Bi, N.; Tang, H.; Shi, Z.; Wang, X.; Han, F.; Liang, J. Effects of Vanadium Microalloying and Intercritical Annealing on Yield Strength-Ductility Trade-offs of Medium-Manganese Steels. *Materials* **2023**, *16*, 2220. [CrossRef] [PubMed]
22. Cai, M.H.; Li, Z.; Chao, Q.; Hodgson, P.D. A novel Mo and Nb microalloyed medium Mn TRIP steel with maximal ultimate strength and moderate ductility. *Metall. Mater. Trans. A* **2014**, *45*, 5624–5634. [CrossRef]
23. Hu, B.; Rong, X.Q.; Tian, C.; Yu, Y.S.; Guo, H.; Misra, R.D.K.; Shang, C.J. Nanoscale precipitation and ultrafine retained austenite induced high strength-ductility combination in a newly designed low carbon Cu-bearing medium-Mn steel. *Mater. Sci. Eng. A* **2021**, *822*, 141685. [CrossRef]
24. Sohn, S.S.; Lee, B.-J.; Kwak, J.-H.; Lee, S. Effects of Annealing Treatment Prior to Cold Rolling on the Edge Cracking Phenomenon of Ferritic Lightweight Steel. *Metall. Mater. Trans. A* **2014**, *45*, 3844–3856. [CrossRef]
25. Zhao, N.; Ding, M.L.; Lin, L.; He, Y.L.; Wang, J.X.; Zhang, R.K.; Zhang, Y.; Liu, R.D.; Wang, L.H.; Li, L. Insights into the relationship between γ/α transformation and strength-ductility of auto-steel with 980 MPa grade based on experiments and theoretical calculations. *Vacuum* **2023**, *215*, 112252. [CrossRef]
26. Li, Z.; Wu, D. Effects of hot deformation and subsequent austempering on the mechanical properties of Si-Mn TRIP steels. *J. Iron Steel Res. Int.* **2006**, *46*, 121–128. [CrossRef]
27. van Dijk, N.H.; Butt, A.M.; Zhao, L.; Sietsma, J.; Offerman, S.E.; Wright, J.P.; van der Zwaag, S. Thermal stability of retained austenite in TRIP steels studied by synchrotron X-ray diffraction during cooling. *Acta Mater.* **2005**, *53*, 5439–5447. [CrossRef]
28. Zhao, L.L.; Wei, S.T.; Wu, D.; Gao, D.B.; Lu, S.P. δ-ferrite transformation mechanism and its effect on mechanical properties of 316H weld metal. Journal of Mater. *Sci. Technol.* **2020**, *57*, 33–42.
29. Yi, H.L.; Ghosh, S.K.; Liu, W.J.; Lee, K.Y.; Bhadeshia, H.K.D.H. Non-equilibrium solidification and ferrite in δ-TRIP steel. *Mater. Sci. Technol.* **2010**, *26*, 817–823. [CrossRef]
30. Sun, B.; Palanisamy, D.; Ponge, D.; Gault, B.; Fazeli, F.; Scott, C.; Yue, S.; Raabe, D. Revealing fracture mechanisms of medium manganese steels with and without delta-ferrite. *Acta Mater.* **2019**, *164*, 683–696. [CrossRef]
31. Hu, B.; Luo, H.W. A strong and ductile 7Mn steel manufactured by warm rolling and exhibiting both transformation and twinning induced plasticity. *J. Alloys Comp.* **2017**, *725*, 684–693. [CrossRef]
32. Caballero, F.G.; Capdevila, C.; de Andrés, C.G. Kinetics and dilatometric behaviour of non-isothermal ferrite–austenite transformation. *Mater. Sci. Technol.* **2001**, *17*, 1114–1118. [CrossRef]
33. Lee, S.; De Cooman, B.C. Influence of Carbide Precipitation and Dissolution on the Microstructure of Ultra-Fine-Grained Intercritically Annealed Medium Manganese Steel. *Metall. Mater. Trans. A* **2016**, *47*, 3263–3270. [CrossRef]
34. Andersson, J.O.; Helander, T.; Höglund, L.; Shi, P.; Sundman, B. Thermo-Calc & DICTRA, computational tools for materials science. *Calphad* **2002**, *26*, 273–312.
35. Luo, H.W.; Shi, J.; Wang, C.; Cao, W.Q.; Sun, X.J.; Dong, H. Experimental and numerical analysis on formation of stable austenite during the intercritical annealing of 5Mn steel. *Acta Mater.* **2011**, *59*, 4002–4014. [CrossRef]
36. Varanasi, R.S.; Lipińska-Chwałek, M.; Mayer, J.; Gault, B.; Ponge, D. Mechanisms of austenite growth during intercritical annealing in medium manganese steels. *Scr. Mater.* **2022**, *206*, 114228. [CrossRef]
37. Arlazarov, A.; Gouné, M.; Bouaziz, O.; Hazotte, A.; Petitgand, G.; Barges, P. Evolution of microstructure and mechanical properties of medium Mn steels during double annealing. *Mater. Sci. Eng. A* **2012**, *542*, 31–39. [CrossRef]

38. Liu, C.Q.; Peng, Q.C.; Xue, Z.L.; Deng, M.M.; Wang, S.J.; Yang, C.W. Microstructure-Tensile Properties Relationship and Austenite Stability of a Nb-Mo Micro-Alloyed Medium-Mn TRIP Steel. *Metals* **2018**, *8*, 615. [CrossRef]
39. Sugimoto, K.I.; Kobayashi, M.; Hashimoto, S.I. Ductility and strain-induced transformation in a high strength TRIP aided dual phase steel. *Metall. Trans. A* **1992**, *23*, 3085–3091. [CrossRef]